Electromagnetic Scattering from Short Branching Vegetation

Tsenchieh Chiu and Kamal Sarabandi
Department of Electrical Engineering and Computer Science
The University of Michigan, Ann Arbor, MI 48109-2122
Tel:(313) 936-1575, Fax:(313) 747-2106
Email: tcchiu@eecs.umich.edu

Abstract – A polarimetric coherent electromagnetic scattering model for short branching vegetation is developed in this paper. With the realistic structures which reasonably describe the relative positions of the particles, this model is able to consider the coherent effect due to the phase difference between the scattered fields from different particles, and account for the second-order near-field interaction between particles to which the relative positions and orientation of the particles are essential. The model validation with measurements is also presented, and excellent agreement is obtained. The polarimetric radar backscatter measurements for soybean plants using truck-mounted scatterometers were conducted at L-band and C-band under different soil-moisture conditions. Through an extensive ground truth, the important plant and rough surface parameters, such as the soil moisture and surface roughness, vegetation dielectric constant, and geometry of the soybean plants, were characterized for model verification. It is found that the second-order near-field scattering is significant at C-band for fully-grown soybeans due to the high vegetation particle density, and at L-band the contribution from the second-order near field is negligible. The coherence effect is shown to be important at L-band and to a much lower extent at C-band. This model is then used to demonstrate its ability for estimating the physical parameters of a soybean field including soil moisture from a polarimetric set of AIRSAR images.

RL-980 = RL-980

1 Introduction

Microwave remote sensing has evolved into an important tool for monitoring the atmosphere and surface of the earth. Electromagnetic waves at microwave frequencies are able to penetrate more deeply into vegetation, and, therefore, retrieving parameters of vegetation and underlying ground surfaces has become one of the major applications of microwave remote sensing. With the advent of polarimetric synthetic aperture radars (SAR) and the development of radar polarimetric techniques, microwave remote sensing has attained significant prominence. While a large amount of data can be collected very efficiently, there are still difficulties in accurately predicting the physical parameters of the targets from the collected radar information. To accomplish this task, a necessary step is to construct a high-fidelity scattering model by which the relationship between all targets' physical parameters to the radar backscatter can be established.

In the early vegetation scattering models, the vegetation medium was simplified in terms of a homogeneous random medium and the single scattering theory was applied to account for the scattering and propagation in the random medium [1, 2, 3]. For example, in [1] a forest stand is represented in terms of a two-layer random medium including a crown layer composed of randomly oriented cylinders and disks representing branches and leaves and a trunk layer containing nearly vertical cylinders representing tree trunks below the crown layer. Although these models are capable of predicting the scattering behavior of vegetation qualitatively, they are incapable of predicting the scattering behavior quantitatively due to their simplifying assumptions. An important feature of a high fidelity scattering model is to preserve the structure of vegetation as different species of vegetation have their own unique structures, which are expected to exhibit their own scattering behaviors. An important effect of the vegetation structure is the coherence effect caused by the relative position of the vegetation particles which produce certain interference pattern. It is shown that the coherence effects caused by the vegetation structure become more significant at lower frequencies [4]. In the remote sensing of vegetation-covered terrain where the underlying soil surface is the target of interest , low microwave frequencies are recommended and therefore the coherence effects must be carefully accounted for. The model developed by Yueh et al. [5] may be among the first to address the coherence effects caused by the vegetation structure. In their scattering model for soybeans, a two-scale branching vegetation structure was constructed, and the scattered fields from particles were added coherently. Lin et al. [6] also proposed a coherent scattering model for forest canopies in which rather realistic tree-like structures are constructed using the fractal theory. In both models, the scattering solutions are formulated using the single scattering theory.

Another important issue in modeling the scattering from vegetation is the effect of the multiple scattering among vegetation particles. Vegetation particles are usually arranged in clusters within a single plant, such as leaves around end branches and branches around main stems and trunks. Therefore, a vegetation medium may be appropriately considered as locally dense. In such cases, the near-field multiple scattering is strong and may significantly affect the overall response. To accurately evaluate the near-field interaction, the realistic description of the relative positions and orientations of the vegetation particles and accurate and efficient scattering formulations are required. In recent years, some advanced scattering solutions that account for the near-field interaction between scatterers have been presented [7, 8]. However, vegetation scattering models which can handle the near-field interaction with realistic vegetation structures have not been developed yet. The evaluation of the near-field interaction is usually numerically intensive, considering the huge number of particles in the medium.

In this paper, a scattering model for soybeans is presented which incorporates realistic computer-generated vegetation structures and accounts for the second-order near-field scattering interaction. Soybeans are erect branching plants composed of components which can be often found in many vegetation: stems, branches, leaves and fruits (pods) arranged in a very well-defined manner. Hence it is very appropriate for studying the effect of the vegetation structure on the radar backscatter. Also because of its moderate number of particles, the computation of the second-order near-field interaction is not formidable. Also from the experimental point of view, the dimensions of soybean plants are small enough to allow for conducting controlled experiments using truck-mounted scatterometers. Due to the uniformity of the plants and underlying soil surface, gathering the ground truth data is rather simple. The paper is organized as follows: Section 2 gives the theoretical description of the model, including the vegetation structure modeling and the scattering solution. In Section 3 the experimental procedures using the University of Michigan truck-mounted scatterometer and AIRSAR are discussed. Finally in Section 4 model validation using the measured data and a sensitivity analysis are presented.

2 Theoretical Analysis

Consider a global coordinate system with x-y plane parallel to a horizontal ground plane and z-axis along the vertical direction, as shown in Fig. 1. Suppose a plane wave given by

$$\mathbf{E}^{\mathbf{i}}(\mathbf{r}) = \mathbf{E}_0^{\mathbf{i}} e^{ik_0 \hat{k}_i \cdot \mathbf{r}} \ . \tag{1}$$

is illuminating the ground plane from the upper half-space, where $\hat{k}_i$ is the unit vector along the propagation direction given by

$$\hat{k}_i = \hat{x} \sin\theta_i \cos\phi_i + \hat{y} \sin\theta_i \sin\phi_i - \hat{z} \cos\theta_i \ . \tag{2}$$

The vector $\mathbf{E}_0^{\mathbf{i}}$ in (1) is expressed in terms of a local coordinate system $(\hat{v}_i, \hat{h}_i, \hat{k}_i)$ where $\hat{h}_i = \hat{k}_i \times \hat{z}/|\hat{k}_i \times \hat{z}|$ and $\hat{v}_i = \hat{h}_i \times \hat{k}_i$ denote the horizontal and vertical unit vectors, respectively. Representing the direction of the observation point by $\hat{k}_s$, the polarization of the scattered field can also be expressed in terms of a local coordinated system $(\hat{v}_s, \hat{h}_s, \hat{k}_s)$ where

$$\hat{k}_s = \hat{x} \sin\theta_s \cos\phi_s + \hat{y} \sin\theta_s \sin\phi_s + \hat{z} \cos\theta_s \ , \tag{3}$$

and $\hat{v}_s$ and $\hat{h}_s$ can be obtained using similar expressions as those given for $\hat{v}_i$ and $\hat{h}_i$, respectively.

2.1 Vegetation Structure Modeling

To make the proposed scattering solution tractable, simple geometries are chosen to represent vegetation particles. Leaves are represented by elliptical thin dielectric disks. The other particles, which include stems, branches, and pods, are modeled using circular cylinders. Analytical scattering solutions are available for both geometries and will be introduced in the next section.

The orientation and dimension of each particle are described by four parameters, as shown in Fig. 2. The values of these parameters are determined by random number generators during the simulation with predescribed probability distribution functions (pdf). The orientation parameters of the particles are described by two angles: β(elevation angle) and γ(azimuth angle). Azimuthal symmetry is assumed for γ, and its pdf is given by

$$p(\gamma) = \frac{1}{2\pi}, \qquad \gamma \in [0, 2\pi) \ . \tag{4}$$

However, for β, a bell-shaped pdf is chosen:

$$p(\beta) = \frac{\epsilon^{-((\beta-\beta_m)/\beta_s)^2}}{\int_0^{\pi} \epsilon^{-((\beta'-\beta_m)/\beta_s)^2}\, d\beta'} , \qquad \beta \in [0, \pi] . \tag{5}$$

For leaves, the axis ratio (b/a) assumed constant and the thickness and major axis (a) are given Gaussian pdfs. Three types of cylinders are considered for main stems, branches, and pods. For these cylinders, Gaussian pdfs are chosen to describe the statistics of their radii and lengths.

The branching structure of soybeans is rather simple and can be developed using the following algorithm:

1. All parameters of main stem are determined using random number generators. The main stem is then divided into subsections, whose lengths are again decided by Gaussian random number generator.

2. At each node (connecting point of two subsections of the stem), a branch is placed whose orientation is obtained from (4) and (5). Depending on the growth stage, pods may be added at each node.

3. To each branch end a leaf is attached. In this paper, the number of leaflets at each branch end is three (this may be different for other soybean species). Azimuthal orientation angle of leaves is determined from the orientation angle of the branches they are connected to.

Figure 9 shows a typical computer-generated soybean structures according to the aforementioned algorithm.

2.2 Scattering Mechanism and Scattering Formulations for the Vegetation Particles and Rough Surfaces

Several scattering mechanisms are considered for the scattering model. Figure 3 depicts 6 different mechanisms including: (1) direct backscatter from the underlying rough surface, (2) direct backscatter from vegetation particles, (3) single ground bounce, (4) double ground bounce, (5) second-order scattering interaction among vegetation particles, and (6) scattering interaction between main stem and the rough surface. The first four mechanisms are included in almost all existing vegetation scattering models. Mechanism #5 is a second-order solution which accounts for the near-field interaction within a single plant. Mechanism #6 is only considered for predicting the cross-polarized scattering at L-band according to a study reported in [10] where it is shown that the co-polarized scattering of mechanism #6 at L-band is weak compared to that of Mechanism #2. Mechanism #6 is also ignored at C-band, because of attenuation experienced by the wave propagating through the vegetation layer. In what follows, the scattering solutions for each mechanism is briefly described.

1. **Mechanism #1:**

   There exist many rough-surface scattering models available in the literature. In this paper, a second-order small perturbation model(SPM) [17] and a physical optic (PO) model [18] are incorporated to handle the backscatter from the rough surface.

2. **Mechanisms #2~#4:**

   These mechanisms are often referred to as the single scattering solutions in which only the scattering solutions for the isolated vegetation particles are considered. The effect of the ground surface in mechanisms #3 and #4 are considered by introducing the ground reflection coefficients. If the SPM is used in mechanism #1, the Fresnel reflection coefficients are used directly. If the PO is needed according to the surface roughness condition, the reflection coefficients are modified by $e^{-2(ks\cos\theta_i)^2}$ to account for the reduction in the surface reflectivity [11]. The single scattering solutions for dielectric disks and cylinders are obtained from the following formulations:

(a) **Elliptical disk:**

The thickness of the soybean leaves ($\approx 0.2 - 0.3mm$) is usually small compared to the wavelength in microwave region and the ratio of the thickness to the diameter of the leaves is much less than unity. Also by noting that the dielectric constant of vegetation is lossy, the Rayleigh-Gans formulation [12] can be applied to derive the scattering solution for the elliptical disks representing the vegetation leaves. For an elliptical disk, the scattering matrix elements are found to be

$$S^d_{pq} = \hat{p} \cdot (\bar{\bar{\mathbf{P}}}_\mathrm{d} \cdot \hat{q}) \frac{A_d k_0^2}{2\pi} \frac{J_1(\sqrt{(aA)^2 + (bB)^2})}{\sqrt{(aA)^2 + (bB)^2}} \,, \tag{6}$$

where A_d, a and b are the area, major axis, and minor axis of the disk respectively. In (6), $\bar{\bar{\mathbf{P}}}_\mathrm{d} = \bar{\bar{\mathbf{U}}}_\mathrm{d}^{-1} \bar{\bar{\mathbf{P}}}_\mathrm{d}^0 \bar{\bar{\mathbf{U}}}_\mathrm{d}$, where $\bar{\bar{\mathbf{P}}}_\mathrm{d}^0$ is the disk's polarizability tensor which can be found in [12, 13], and $\bar{\bar{\mathbf{U}}}_\mathrm{d}$ is the matrix of coordinate transformation which transfers the global coordinate system to a local coordinate system defined by the major axis, minor axis, and the normal of the disk respectively. The explicit expression for $\bar{\bar{\mathbf{U}}}_\mathrm{d}$ can be obtained from [14]. Also A and B are given by

$$\begin{aligned} A &= k_0 \left[\bar{\bar{\mathbf{U}}}_\mathrm{d}^{-1} \cdot (\hat{k}_i - \hat{k}_s) \right] \cdot \hat{x} \\ B &= k_0 \left[\bar{\bar{\mathbf{U}}}_\mathrm{d}^{-1} \cdot (\hat{k}_i - \hat{k}_s) \right] \cdot \hat{y} \,. \end{aligned} \tag{7}$$

(b) **Circular cylinder:**

Exact scattering solution does not exist for cylinders of finite length, but an approximated solution, which assumes the internal field induced within the finite cylinder is the same as that of the infinite cylinder with the same cross section and dielectric constant, can be used [15]. Generally, this solution is valid when the ratio of the length to the diameter is large.

3. **Mechanism #5:**

The second-order scattered field between two particles is formulated using an efficient algorithm based on the reciprocity theorem [7]. For two adjacent particles we have

$$\hat{p} \cdot \mathbf{E}_{21} = \int_{V_1} \mathbf{E}_{e2} \cdot \mathbf{J}_1 \, dv \,. \tag{8}$$

where $\mathbf{E}_{e2}$ is the scattered field from particle #2 illuminated by an infinitesimal current source at the observation point in the absence of particle #1, and $\mathbf{J}_1$ is the induced polarization current of particle #1 illuminated by the incidence field in the absence of particle #2. $\mathbf{E}_{12}$ can be obtained using the reciprocity theorem. Hence the second-order scattered field are conveniently obtained from the plane wave solution of the induced polarization current and near field of individual particles. These quantities for disks and cylinders are given by:

(a) **Disk:** The induced polarization current is obtained from Rayleigh-Gans approximation and is given by

$$\mathbf{J}_1(\mathbf{r}) = -ik_o Y_o \bar{\bar{\mathbf{P}}}_\mathrm{d} \cdot \mathbf{E}_0^\mathrm{i} e^{ik_o \hat{k}_i \cdot \mathbf{r}} . \tag{9}$$

where $\bar{\bar{\mathbf{P}}}_\mathrm{d}$ is the polarizability tensor. The exact near-field scattered field must be numerically evaluated from

$$\mathbf{E}_{\mathrm{e}2}(\mathbf{r}) = \frac{ik_0 Z_0}{(4\pi)^2} \frac{e^{ik_0 r_0}}{r_0} \left(\bar{\bar{\mathbf{P}}}_\mathrm{d} \cdot \hat{p} \right) \cdot \int_{S_2} \bar{\bar{\mathbf{G}}}(k, R) e^{ik_0(-\hat{k}_s \cdot \mathbf{r}' + R)} \, ds' , \tag{10}$$

where

$$\bar{\bar{\mathbf{G}}}(k_0, R) = \left(\frac{-1 + ik_0 R + k_0^2 R^2}{R^3} \right) \bar{\bar{\mathbf{I}}} + \left(\frac{3 - 3ik_0 R - k_0^2 R^2}{R^3} \right) \hat{R}\hat{R} , \tag{11}$$

and $\hat{R}$ is a unit vector defined by $\hat{R} = (\mathbf{r} - \mathbf{r}')/|\mathbf{r} - \mathbf{r}'|$.

(b) **Cylinder:** The formulation for finite finite cylinders is used again to calculate the induced polarization current and the near-field scattered field. The formulation of the scattered field in the vicinity of the cylinder is given by [7]

$$\mathbf{E}_{\mathrm{e}2}(\mathbf{r}) = -\frac{ik_o Z_o e^{ik_o r_o}}{4\pi r_o} \mathbf{F}(\phi - \phi_s) H_o^{(1)}(k_o \sin\theta_s \rho) e^{k_o \cos\theta_s z} . \tag{12}$$

Equation (12) is derived using the stationary phase approximation along the axial direction of the cylinder axis. This solution has been verified by the method of moments [7, 16], and the region of validity is given by

$$\rho > 2d_c^2/\lambda , \tag{13}$$

where d_c is the diameter of the cylinder, and ρ is the radial distance between the observation point and the cylinder axis. For the main stem of soybeans, the radius is usually less than 5mm. Applying (13) it is found that $\rho > 3.5mm$ at C-band (5.3 GHz). Therefore, (12) is appropriate for calculating the near-field interaction.

4. **Mechanism #6:**

The incoherent interaction between the main stems and rough surface is formulated using the reciprocity technique introduced in [7]. The details and lengthy formulation for the cylinder-rough surface scattering interaction can be found in [19]. This model is only applied to calculate the scattering interaction between the main stem and underlying rough surface. The reason for this is that for a titled cylinder with large elevation angle (β) such as branches, the cross-polarized scattering from mechanisms #2 and #3 is dominant. However, main stems often grow nearly vertically and its interaction with the ground becomes a important source of the cross-polarized scattering, noting that the mechanisms #2 and #3 of nearly vertical cylinders do not produce significant cross-polarized scattering field. As will be shown later, the cross-polarized scattering at L-band is mainly dominated by two scattering mechanisms #2 and #6.

2.3 Propagation in a Lossy Layered Media

2.3.1 Foldy's Approximation

The scattering solutions provided in the previous section are for targets in free space. However, for vegetation canopies the targets are within a lossy random medium. Thus, a particle is illuminated by not only the incident plane wave, but also by the scattered fields from other particles. To calculate the total scattered field from a particle, it is usually assumed that the particle is embedded in homogeneous lossy medium, as shown in Fig. 4(a). The vegetation layer can be divided into many sub-layers which contain different types and number density of vegetation particles, and thus each layer exhibits different equivalent propagation constants.

Foldy's approximation [14] has been widely used in many vegetation scattering models to account for the attenuation experienced by the wave traveling through the vegetation medium. According to the Foldy's approximation the vertical and horizontal components of the mean electric field in a sparse random medium satisfy

$$\begin{aligned} \frac{dE_h}{ds} &= i\left(k_0 + M_{hh}\right)E_h + iM_{hv}E_v \\ \frac{dE_v}{ds} &= iM_{vh}E_h + i\left(k_0 + M_{vv}\right)E_v \ , \end{aligned} \tag{14}$$

where s is the length along the propagation path within the medium and

$$M_{pq} = \frac{2\pi n_0}{k_0}\langle S_{pq}(\hat{k},\hat{k})\rangle \ , \qquad p,q \in \{h,v\} \ . \tag{15}$$

Here n_0 is the number density of the scatterers within the medium, and $\langle S_{pq}(\hat{k},\hat{k})\rangle$ is the averaged forward scattering matrix element of the scatterers. Since the vegetation structure exhibits statistical azimuthal symmetry, there is no coupling between horizontal and vertical components of the coherent field and therefore $M_{hv} = M_{vh} = 0$. From (14), the effective propagation constants for both polarizations are given by

$$\begin{aligned} k_h^e &= k_0 + M_{hh} \\ k_v^e &= k_0 + M_{vv} \ . \end{aligned} \tag{16}$$

As mentioned previously, the second-order near-field interaction is incorporated in this model, and it will only be calculated for the scatterers within a single plant. It is reasonable to assume that no extinction should be considered for the calculation of the near-field interaction. However, since both particle are still embedded in the vegetation layer, extinction is considered for the incident wave and secondary scattered fields. As shown in Fig. 4(b), the space between two scatterers is considered as free space, and Foldy's approximation is still used on paths #1 and #2.

2.3.2 Propagation Paths

In this section, the phase difference and extinction caused by the wave propagating in the vegetation layer will be formulated using the method presented in [20]. To build a coherent scattering model, the phase of each scattering mechanism has to be calculated with respect to a phase reference point. Figure 5(a) shows the propagation geometry for the direct path. The reference phase point is taken to be the origin of the coordinate system. Using ray optics, the propagation from the equi-phase plane (shown in Fig. 5(a)) directly to the scatterer is given by

$$\Phi_d'(\hat{k}_0, \mathbf{r}', p) = k_0\mathbf{r}_1 \cdot \hat{k}_0 + k_p^e(\mathbf{r}' - \mathbf{r}_1) \cdot \hat{k}_e \ , \tag{17}$$

where $\mathbf{r}_1$ denotes the location where the ray intersects the interface between the vegetation layer and free-space. Here the effect of refraction is ignored assuming a diffuse boundary between the vegetation layer and free-space ($\hat{k}_\epsilon = \hat{k}_0$) and p denotes the polarization of the wave. Substituting (16) into (17), it is found that

$$\Phi'_d(\hat{k}_0, \mathbf{r}', p) = k_0 \mathbf{r}' \cdot \hat{k}_0 + M_{pp}(\mathbf{r}' - \mathbf{r}_1) \cdot \hat{k}_0 \ . \tag{18}$$

The first term on the right-hand side of (18) is the free-space propagation term and will be included in the scattering matrix elements of the scatterer. The second-term on the right-hand side is the extra phase difference and extinction caused by the propagation in the lossy vegetation media, and will be denoted as $\Phi_d(\hat{k}_0, \mathbf{r}', p)$. The free space-vegetation interface is set to be the x-y plane, so it is found that

$$(\mathbf{r}' - \mathbf{r}_1) \cdot \hat{k}_0 = \frac{z'}{\hat{k}_o \cdot \hat{z}} \ . \tag{19}$$

Therefore, $\Phi_d(\mathbf{r}', p)$ can be written as

$$\Phi_d(\hat{k}_0, \mathbf{r}', p) = M_{pp} \frac{z'}{\hat{k}_o \cdot \hat{z}} \ . \tag{20}$$

The ground-bounce path, as shown in Fig. 5(b), includes a reflection from the ground plane. In Fig. 5(b), the image position is given by

$$\mathbf{r}'_{image} = x'\hat{x} + y'\hat{y} - (z' + 2d)\hat{z} \ , \tag{21}$$

where d is the thickness of the layer. Using (20), it is found that $\Phi_g(\hat{k}_0, \mathbf{r}', p)$, which only accounts for the extra phase difference and extinction caused by the propagation in the lossy vegetation media, can be written as

$$\Phi_g(\hat{k}_0, \mathbf{r}', p) = -M_{pp} \frac{z' + 2d}{\hat{k}_o \cdot \hat{z}} \ . \tag{22}$$

2.4 Scattering from Soybean Fields and Monte-Carlo Simulation

Consider an area of soybean field with N_p soybean plants per unit area. For a given computer-generated soybean plant (the k-th plant with N_s particles), the total scattering amplitude can be written as

$$S_{pq,k} = \left\{ \sum_{i=1}^{N_s} \left[S^d_{pq,ki} + S^{gg}_{pq,ki} + S^{g1}_{pq,ki} + S^{g2}_{pq,i} \right] + \sum_{i=1}^{N_s} \sum_{\substack{j=1 \\ j \neq i}}^{N_s} S^{2nd}_{pq,kij} \right\} e^{ik_0(\hat{k}_i - \hat{k}_s) \cdot \mathbf{r}_\mathbf{k}} \ , \tag{23}$$

where $\mathbf{r}_\mathbf{k}$ is the location of the plant. In (23) each term includes the attenuation and phase shift due to the propagation:

$$\begin{aligned} \text{direct:} \qquad & S^d_{pq,ki} = S_{pq,ki}(\hat{k}_s, \hat{k}_i) e^{i\Phi_d(-\hat{k}_s, \mathbf{r}_{ki}, p)} e^{i\Phi_d(\hat{k}_i, \mathbf{r}_{ki}, q)} \\ \text{ground-plant:} \qquad & S^{g1}_{pq,ki} = S_{pq,ki}(\hat{k}_s, \hat{k}'_i) R_p e^{i\Phi_g(-\hat{k}_s, \mathbf{r}_{ki}, p)} e^{i\Phi_d(\hat{k}_i, \mathbf{r}_{ki}, q)} \\ \text{plant-ground:} \qquad & S^{g1}_{pq,ki} = S_{pq,ki}(\hat{k}'_s, \hat{k}_i) R_q e^{i\Phi_d(-\hat{k}_s, \mathbf{r}_{ki}, p)} e^{i\Phi_g(\hat{k}_i, \mathbf{r}_{ki}, q)} \\ \text{ground-ground:} \qquad & S^{gg}_{pq,ki} = S_{pq,ki}(\hat{k}'_s, \hat{k}'_i) R_q R_q e^{i\Phi_g(-\hat{k}_s, \mathbf{r}_{ki}, p)} e^{i\Phi_g(\hat{k}_i, \mathbf{r}_{ki}, q)} \\ \text{near-field 2nd-order:} \qquad & S^{2nd}_{pq,kij} = S^{2nd}_{pq,kij}(\hat{k}_s, \hat{k}_i) e^{i\Phi_d(-\hat{k}_s, \mathbf{r}_{ki}, p)} e^{i\Phi_d(\hat{k}_i, \mathbf{r}_{kj}, q)} \ , \end{aligned} \tag{24}$$

where $\hat{k}_i' = \hat{k}_i - 2(\hat{k}_i \cdot \hat{z})\hat{z}$ and $\hat{k}_s' = \hat{k}_s - 2(\hat{k}_s \cdot \hat{z})\hat{z}$. Note that all scattering mechanisms are added coherently to capture the coherence effect caused by the vegetation structure.

The scattering coefficient of the soybean field is then computed by incoherent addition of the scattered powers from vegetation, rough surface, and main stem-rough surface interaction. Hence

$$\sigma^0_{pqpq} = \sigma^0_{pqpq}(\text{vegetation}) + \sigma^0_{pqpq}(\text{rough surace}) + \sigma^0_{pqpq}(\text{stem-rough surface}) \, , \tag{25}$$

where

$$\sigma^0_{pqpq}(\text{vegetation}) = 4\pi \left\langle \left| \sum_{k=1}^{N_p} S_{pq,k} \right|^2 \right\rangle \tag{26}$$

$$\sigma^0_{pqpq}(\text{rough surface}) = \sigma^0_{pqpq,r} \left| e^{i\Phi_d(-\hat{k}_s, -d\hat{z}, p)} e^{i\Phi_d(\hat{k}_i, -d\hat{z}, q)} \right|^2 \tag{27}$$

$$\begin{aligned} \sigma^0_{pqpq}(\text{stem-rough surface}) = 4\pi N_p \Big\langle \Big| & S^{rc}_{pq} e^{i\Phi_d(-\hat{k}_s, -d\hat{z}, p)} e^{i\Phi_d(\hat{k}_i, (-d+0.5l_c)\hat{z}, q)} \\ & + S^{cr}_{pq} e^{i\Phi_d(\hat{k}_i, -d\hat{z}, p)} e^{i\Phi_d(-\hat{k}_s, (-d+0.5l_c)\hat{z}, q)} \Big|^2 \Big\rangle \, . \end{aligned} \tag{28}$$

In calculation of the contribution from the direct rough surface and the stem-rough surface, the propagation attenuation through vegetation layer is also included. S^{rc}_{pq} and S^{cr}_{pq} are, respectively, the rough surface-cylinder and cylinder-rough surface scattering amplitudes. The ensemble averaging in (28) is carried out analytically using the SPM formulation, and the details are reported in [10]. As mentioned earlier, the contribution from this term is only significant at L-band for the cross-polarized term.

The ensemble averaging in (26) is carried out using a Monte-Carlo simulation. For each realization in the Monte-Carlo simulation, a group of computer-generated soybean plants are generated and distributed on a square area of 1 m^2, and then the scattered fields are computed. This procedure will be repeated until a convergence is reached. To examine the coherence effect, the scattered power from the vegetation is also calculated incoherently from

$$\begin{aligned} \sigma^0_{pqpq}(\text{vegetation}) = 4\pi \Bigg\langle \sum_{k=1}^{N_p} \Bigg\{ & \sum_{i=1}^{N_s} \left[\left| S^{d}_{pq,ki} \right|^2 + \left| S^{gg}_{pq,ki} \right|^2 + \left| S^{g1}_{pq,ki} \right|^2 + \left| S^{g2}_{pq,i} \right|^2 \right] \\ & + \sum_{i=1}^{N_s} \sum_{\substack{j=1 \\ j \neq i}}^{N_s} \left| S^{2nd}_{pq,kij} \right|^2 \Bigg\} \Bigg\rangle \, . \end{aligned} \tag{29}$$

3 Experimental Results

In this section, the experimental procedure and the multi-frequency multi-polarization backscatter measurements using polarimetric scatterometer systems and JPL AIRSAR are presented.

3.1 Measurement Using the University of Michigan's POLARSCAT

In August of 1995, a series of polarimetric measurements were conducted on a soybean field near Ann Arbor, MI. These measurement were conducted using the University of Michigan polarimetric scatterometer systems (POLARSCAT) [21]. The polarimetric backscatter data were collected at two different frequencies (L-band and C-band) over a wide range of incidence angles (from 20^o to 70^0 at 10^o increment). The overall goal of these experiments was to investigate the feasibility of soil-moisture retrieval of vegetation-covered terrain from radar backscatter data. Experiments were designed to observe the radar-backscatter variations due to the change in soil moisture while the vegetation parameters were almost the same. Two sets of data were collected. In one measurement the angular polarimetric data were collected on August 14 when the underlying soil surface was dry, and in another a similar data was collected right after a heavy rain on August 18. At the time of experiments the soybean plants were fully grown with significant number of pods. In fact the vegetation biomass was at its maximum. Since the separation between the time of experiments were only about 4 days, no significant change in the vegetation parameters were observed.

The vegetation structural parameters and moisture in addition to the soil surface roughness and moisture were carefully characterized. The dielectric constant of the soil surface was measured by using a C-band field-portable dielectric probe [22]. The measured relative dielectric constant (ϵ_r) was used to estimate the moisture contents (m_v) by inverting a semi-empirical model [23] which give ϵ_r in terms of m_v. The mean m_v, which is shown in Table 1, is then used to estimate ϵ_r at L-band.

Two dielectric measurement techniques [24, 25] were used to measure the dielectric constant of leaves and stems. These measurement were performed at C-band using WR-187 waveguide sample holder, and the results are shown in Fig. 6. The corresponding dielectric constants at L-band was then calculated using the empirical model provided in [26]. The gravimetric moisture content (m_g) of the vegetation was also measured on the day of radar measurement to monitor the variation of the biomass. As shown in Table 1, the vegetation moisture remained almost the same on both dates of the experiments.

The dimensions and orientations of vegetation particles were also recorded. Table 2 shows the means and standard deviations of vegetation parameters. Unlike most cultivated fields where the plants are planted in row structures, the soybean plants of this field were distributed in a rather random pattern, as shown in Fig. 7. This picture shows the top-view at the end of the season where all the leaves were fallen. The surface roughness parameters were also measured and reported in Table 1.

3.2 Measurement Using AIRSAR

JPL Airborne Synthetic Aperture Radar (AIRSAR) [27] was deployed to conduct backscatter measurements on a number of cultivated fields. Although AIRSAR is capable of measuring polarimetric backscatter at three microwave frequencies (P-,L-, and C-band), only L-band and C-band data were collected. The backscatter data were collected by AIRSAR during its flight over the Kellogg Biological Station near Kalamazoo, Michigan, on July 12, 1995. Also these data sets were collected at three different incidence angles: 30, 40, 45 degree. Unfortunately the soybean fields were not within the research site of the station and the ground truth data was rather limited. The only available informations are that the soybean were about a month old and the volumetric soil moisture content was less than 0.1. Figure 8 shows the composite L-band and C-band SAR image at 45^o incidence angle.

4 Data Simulation and Analysis

The vegetation scattering model is first validated using the data collected by POLARSCAT. Guided by the ground truth data, many soybean plant structures were generated in order to carry on the data simulation (see Fig. 9(a)). The computer-generated plants were uniformly distributed using a random number generator. The Monte-Carlo simulations are performed at incidence angles ranging from 20^o to 70^o at 5^o increment. Figures 10(a) and 11(a) show the simulated and measured backscattering coefficients versus incidence angle at L-band and C-band, respectively. Good agreement is achieved by allowing the dielectric constants of vegetation particles vary within the confidence region shown in Fig. 6. In figures 10(b), (c), and (d), the contributions from individual scattering mechanisms are plotted as functions of incidence angle at L-band. The cross products of among different mechanisms, which account for the coherence effect, are not presented in these figures. It is quite obvious that the contribution from the second-order near-field interaction at L-band is negligible for both co- and cross-polarized terms. It is also shown that for co-polarized backscattering coefficient the direct backscatter from soybean, direct backscatter from rough surface, and single ground-bounce are sufficient to characterize the scattering behavior. For cross-polarization, however, the two most significant mechanisms are the direct backscatter from vegetation and the incoherent rough surface-stem interaction. The later mechanism contains information regarding the underlying soil surface including the soil moisture. Figures 11(b), (c), and (d) show scattering contributions from different mechanisms versus incidence angle at C-band. The direct backscatter form vegetation and the second-order near-field interaction are the dominant scattering mechanisms at C-band. Because of larger near-field region, the near-field interaction is stronger at C-band than at L-band. Also the second-order near-field interaction has more profound effect on the vv- and cross-polarization, because the orientation of the main stems is nearly vertical. The other mechanisms, which include the soil moisture information, are not significant for two reasons: (1) high extinction through the vegetation layer, and (2) surface roughness which decreases the reflectivity of the ground surface.

From these analysis it is found that the backscatter at C-band or higher frequencies are mainly sensitive to vegetation parameters for sufficiently high vegetation biomass (in this case, biomass = 1.97 kg/m^2). At L-band or lower frequencies, it is possible to sense the soil moisture for surfaces covered with short vegetation and relatively high biomass. Figures 12(a), (b), and (c) demonstrate the sensitivity of the backscatter to soil moisture as a function of incidence angle for the soybean field. The simulations are performed under four different soil-moisture conditions: $m_v = 0.1, 0.2, 0.3$ and 0.4 at L-band. The backscatter data collected on August 14 and August 18 are also plotted in these figures for comparison. These results suggest that the appropriate range of incidence angle for the the purpose of soil-moisture retrieval is $\theta_i < 50^o$ where there is about 6-dB of dynamic range. At incidence angles larger than 50^o, the sensitivity to soil moisture decreases due to the high extinction caused by the vegetation. To retrieve the soil moisture accurately, vegetation parameters must be estimated as accurately as possible. It seems a combination of high and low frequency backscatter data is needed to estimate the vegetation and soil moistures accurately.

Due to the limited ground-truth data, the AIRSAR data set is used for estimating the vegetation and surface roughness parameters. Although the retrieval algorithm presented here is based on trial and error, it indicates the feasibility of estimating vegetation parameters and soil moisture from image radars. The procedure for estimating these parameters is described below:

1. Based on a series of trial simulations, it is found that the second-order near-field interaction can be ignored at L- and C-band for the one-month old soybeans. In this case the soybean plants are still young with shorter branches and stems and much fewer number of vegetation particles. Also there are no pods on the plants whose interaction with the

main stem is the major source of the near-field interaction.

2. Judging from the measured values of the co-polarized scattering coefficients reported in Fig. 13(a), it is inferred that the vegetation biomass is rather low. In this case, depending on the surface roughness, the surface scattering mechanism can be dominant at low incidence angles. If the surface scattering is dominant entirely, it is expected that σ_{vv}^{o} be larger than σ_{hh}^{o}. However, this is not observed from the measured data at 30°. Hence, there is at least a comparable backscattering contribution from the vegetation. Under this condition, a significant contribution to the backscatter at C-band comes from the vegetation.

3. At relatively low biomass, it is found that cross-polarized scattering coefficient is dominated by the direct backscatter from the soybean at both frequency bands. The size of the main stems for one-month-old soybean is small, so the rough surface-stem interaction is not significant. Also at C-band the direct backscatter from the rough surface is weak due to the small rms height and extinction through the vegetation layer. Therefore, the dimension, the number density, and the dielectric constant of the soybean can be estimated by matching the cross-polarized backscatter at C-band. This is done by confining the range of the vegetation dielectric constants to those reported in Fig. 6. The elevation angles of all vegetation particles can be estimated by matching the co-polarized scattering coefficient ratio $\sigma_{vv}^{0}/\sigma_{hh}^{0}$ and cross-polarized scattering coefficient. The vegetation parameters as a first iteration is decided by matching the data at C-band. Then, by matching the data at L-band with the same vegetation structure, the parameters of the rough surface is estimated. The simulation is then iterated between L-band and C-band until the simulated and measured data match at both frequency bands.

After matching the backscatter data at both L- and C-band, the final estimated target parameters are shown in Tables 3 and 4. A typical corresponding computer-generated soybean plant is shown in Fig. 9(b). Figures 13(a) and 14(a) show the simulated and measured scattering coefficients versus incidence angle at L- and C-band, respectively. Monte-Carlo simulation are performed at 5 degree increments. Figures 13(b), (c), and (d) show scattering contributions from different mechanisms versus incidence angle at L-band. As predicted, the scattering between stems and rough surface is not significant due to the shorter and slimmer main stems and smaller surface roughness. Figures 13(b), (c), and (d) show scattering contributions from different mechanisms versus incidence angle at C-band. As predicted, the second-order scattering can be neglected.

Finally, Figs. 15 and 16 show the coherence effect of the vegetation structure. The scattering coefficients do not include the contribution from the main stems-rough surface scattering and the direct backscatter from the rough surface. In these figures the coefficients denoted as "coherent" are calculated using (26), while those which are denoted as "incoherent" are calculated using (29). It is shown that for a fully grown soybean, the coherence effect is significant at L-band for co-polarized components, while the effect is not observable at C-band. However, for low biomass condition (AIRSAR data), it is found that the coherent effect is also significant at C-band. This can be explained noting that a fully-grown soybean plant has more complex structure with more particles than a one-month-old plant. Nevertheless, it should be noted that the second-order near-field interaction is significant for POLARSCAT data at C-band, and can be evaluated only when the relative distance and orientation of particles are given. Therefore, to some extent, the coherence effect of structure embedded in this mechanism is also important at C-band. For the cross-polarized scattering, the coherence effect is less significant in both low and high biomass conditions at both frequencies.

5 Conclusions

In this paper, an electromagnetic scattering model for short branching vegetation is presented. The vegetation particles are modeled as simple geometries such as cylinders and disks for which analytical scattering solutions are available. With the realistic structures which reasonably describe the relative positions of the particles, this model is is constructed so that the coherence effect due to the phase difference between the scattered fields from different particles and the second-order near-field interaction among particles are accounted for. Also the interaction between the main stems and underlying rough surface is incorporated into this model which is shown to be important only at low frequencies (L-band) and for cross-polarized backscattering coefficient.

The model accuracy is verified using polarimetric radar backscatter measurements of a soybean field obtained from truck-mounted scatterometers. Through an extensive ground-truth data collection, target parameters such as the soil and vegetation moisture contents, geometry of the soybean plants, and surface roughness were characterized. Monte-Carlo simulations were carried out simulating the statistical properties of the backscatter at different incidence angles. Good agreement is obtained between the model prediction and measured backscattering coefficients. From a sensitivity analysis, it is found that: (1) the second-order near-field interaction is more significant at C-band than at L-band, (2) the interaction between the main stems and rough surfaces could be significant for cross-polarized scattering at L-band, (3) the double ground-bounce mechanism is generally not important, and (4) high-frequency data (C-band or higher) can be used to probe the vegetation, and low-frequency data (L-band or lower) is needed to probe the soil moisture through vegetation.

The model was also used to estimate the parameters of a soybean field using the AIRSAR data, and reasonable results which agree with the limited ground-truth data was obtained. The coherence effect was also examined using the model simulation.

Acknowledgment: This research was supported by NASA under contract NAGW-4180 and JPL under contract JPL-958749.

References

[1] Ulaby, F.T., K. Sarabandi, K. McDonald, M. Whitt, and M.C. Dobson, "Michigan microwave canopy scattering model," *Int. J. Remote Sensing*, vol. 11, no. 7, pp. 2097-2128, 1990.

[2] Karam, M.A. and A.K. Fung,"Electromagnetic scattering from a layer of finite length, randomly oriented, dielectric circular cylinders over a rough interface with application to vegetation," *Int. J. Remote Sensing*, vol. 9, pp. 1109-1134, 1988.

[3] Lang, R.H. and J.S. Sidhu,"Electromagnetic backscattering from a layer of vegetation: a discrete approach," *IEEE Trans. Geosci. Remote Sensing,* vol. 21, pp. 62-71, 1983.

[4] Zhang G., L. Tsang, and Z. Chen, "Collective scattering effects of trees generated by stochastic Lindenmayer systems," *Microwave and Optical Technology Letters,* vol 11, no. 2, pp. 107-111, Feb. 1995.

[5] Yueh, S.H., J.A. Kong, J.K. Jao, R.T. Shin, and T.L. Toan, "Branching model for vegetation," *IEEE Trans. Geosci. Remote Sensing,* vol. 30, no. 2, pp. 390-402, March 1992.

[6] Lin, Y.C. and K. Sarabandi, "A Monte Carlo Coherent Scattering model for forest canopies using fractal generated trees," to be submitted to *IEEE Trans. Geosci. Remote Sensing.*

[7] Sarabandi, K. and P.F. Polatin, "Electromagnetic scattering from two adjacent objects," *IEEE Trans. Antennas Propagat.*, vol. 42, no. 4, pp. 510-517, 1994.

[8] Tsang L., K. Ding, G. Zhang, C.C. Hsu, and J.A. Kong, "Backscattering enhancement and Clustering effects of randomly distributed dielectric cylinders overlying a dielectric half space based on Monte-Carlo simulations," *IEEE Trans. Antennas Propagat.*, vol. 43, no. 5, pp. 488-499, May 1995.

[9] Raven, P.H., R.F. Evert, and S.E. Eichhorn, *Biology of Plants*, Worth Publishers, INC., New York, NY, 1986.

[10] Chiu, T. and K. Sarabandi, "Electromagnetic scattering interaction between a dielectric cylinder and a slightly rough surface," submitted to *IEEE Trans. Antennas Propagat.*.

[11] Ishimaru A. *Wave Propagation and Scattering in Random media,* vol. 2, New York: Academic, 1978.

[12] Schiffer, R. and K.O. Thielheim, "Light Scattering by Dielectric Needles and Disks," *J. Appl. Phys.*, 50(4), April 1979.

[13] Sarabandi, K. and T.B.A. Senior, "Low-frequency Scattering from Cylindrical Structures at Oblique Incidence," *IEEE Trans. Geosci. Remote Sensing*, vol. 28, no. 5, pp. 879-885, 1990.

[14] Tsang, L., J. Kong, and R.T. Shin, *Theory of Microwave Remote Sensing*, John Wiley and Sons, New York, 1985.

[15] Seker S.S. and A. Schneider, "Electromagnetic Scattering from a dielectric cylinder of finite length," *IEEE Trans. Antennas Propagat.*, vol. 36, no. 2, pp. 303-307, Feb. 1988.

[16] Polatin P.F., K. Sarabandi, and F.T. Ulaby, "Monte-Carlo simulation of electromagnetic scattering from a heterogeneous two-component medium," *IEEE Trans. Antennas Propagat.*, vol. 43, no. 10, pp. 1048-1057, Oct. 1995.

[17] Sarabandi K. and T. Chiu, "Electromagnetic scattering from slightly rough surface with inhomogeneous dielectric profiles," *IEEE Trans. Antennas Propagat.*, vol. 45, no. 9, pp. 1419-1430, Sep. 1997.

[18] Ulaby F.T., R.K. More, and A.K. Fung, *Microwave Remote Sensing: Active and Passive*, vol. 2, Artech House, Norwood, MA., 1982.

[19] Chiu T. and K. Sarabandi, "Electromagnetic scattering interaction between a dielectric cylinder and a slightly rough surface," submitted to *IEEE Trans. Antennas Propagat.*.

[20] Stiles J., *A coherent polarimetric microwave scattering models for grassland structures and canopies*, Ph.D. dissertation, the University of Michigan, Ann Arbor, 1996.

[21] Tassoudji M.A., K. Sarabandi, and F.T. Ulaby, "Design consideration and implementation of the LCX polarimetric scatterometer (POLARSCAT)," Rep. 022486-T-2, Radiation Laboratory, The University of Michigan, June 1989.

[22] Brunfeldt D.R., "Theory and design of a field-portable dielectric measurement system," *IEEE Int. Geosci. Remote Sensing Symp. (IGARSS) Digest*, vol. 1, pp. 559-563, 1987.

[23] Hallikainen M.T., F.T. Ulaby, M.C. Dobson, M.A. El-Rayes, and L. Wu, "Microwave dielectric behavior of wet soil - Part I: Empirical models and experimental observations," *IEEE Trans. Geosci. Remote Sensing*, vol. GE-23, pp. 25-34, 1985.

[24] Sarabandi K. and F.T. Ulaby, "Technique for measuring the dielectric constant of thin materials," *IEEE Trans. Instrum. Meas*, vol. 37, no. 4, pp. 631-636, Dec. 1988.

[25] Sarabandi K., "A technique for dielectric measurement of cylindrical objects in a rectangular waveguide," *IEEE Trans. Instrum. Meas*, vol. 43, no. 6, pp. 793-798, Dec. 1994.

[26] Ulaby F.T. and M.A. El-Rayes, "Microwave dielectric spectrum of vegetation, part II: Dual-dispersion model," *IEEE Trans. Geosci. Remote Sensing*, vol. GE-25, pp. 550-557, 1987.

[27] http://www.jpl.nasa.gov/mip/airsar.html

	Aug. 14	Aug. 18
soil (m_v)	0.06	0.17
rms height(s)	$0.0115m$	
correlation length(l)	$0.0879m$	
vegetation (m_g)	0.769	0.767
number density of plant	34 ± 13 plants/m^2	
biomass	1.97 kg/m^2	

Table 1: Measured ground truth for the POLARSCAT data set.

	β_m, β_s (degree)	radius (cm)	length or thickness (cm)
stem	5, 5	0.3 ± 0.09	73.0 ± 3.4
node	5, 5	0.3 ± 0.09	5.4 ± 1.4
branch	45.8, 25.6	0.12 ± 0.031	20.7 ± 6.5
pod	135.5, 30.8	0.35 ± 0.03	3.7 ± 0.48
leaf	45.6, 30.1	$3.8 \pm 0.07(0.576)$	0.022 ± 0.002

Table 2: Measured vegetation parameters of soybeans for the POLARSCAT data set.

soil (m_v)	0.05
rms height(s)	0.0038 m
correlation length(l)	0.038 m
number density of plant	19 plants/m^2
biomass	0.22 kg/m^2

Table 3: Estimated ground truth for the AIRSAR data set.

	β_m, β_s (degree)	radius (cm)	length or thickness (cm)
stem	7.5, 5	0.18 ± 0.05	30.2 ± 3.4
node	7.5, 5	0.18 ± 0.05	5.0 ± 1.0
branch	60.8, 25.6	0.12 ± 0.031	14.7 ± 4.5
leaf	47.0, 30.0	$3.7 \pm 0.08(0.6)$	0.02 ± 0.001

Table 4: Estimated vegetation parameters of soybeans for the AIRSAR data set.

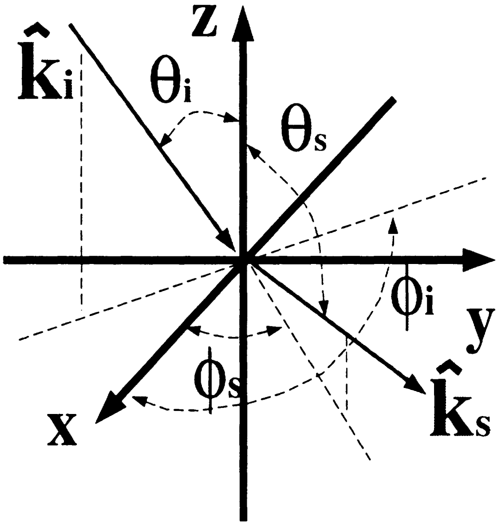

Figure 1: Definition of the incident and scattering angles.

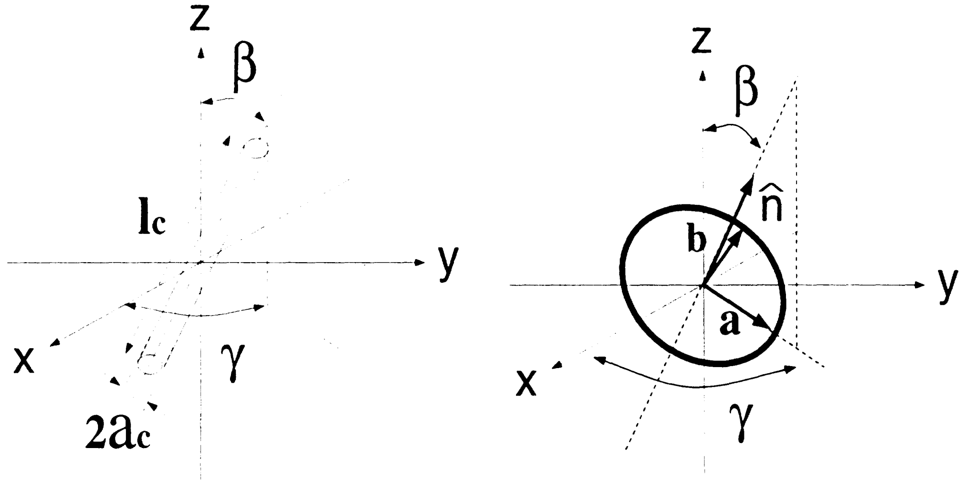

(a) (b)

Figure 2: Denotation of the dimensional and orientational parameters for (a) a cylinder and (b) a disk.

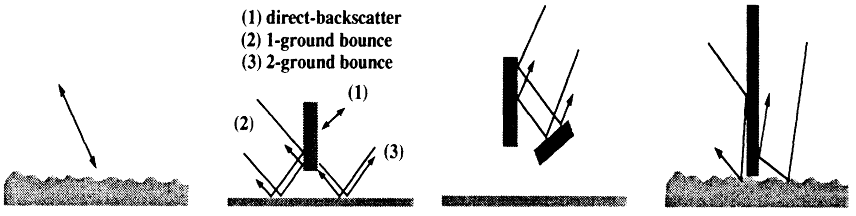

(a) (b) (c) (d)

Figure 3: Scattering mechanisms. (a) direct backscatter from rough surface, (b) direct backscatter from vegetation, single ground-bounce, and double ground-bounce, (c) second-order near-field interaction, and (d) incoherent main stem-rough surface interaction.

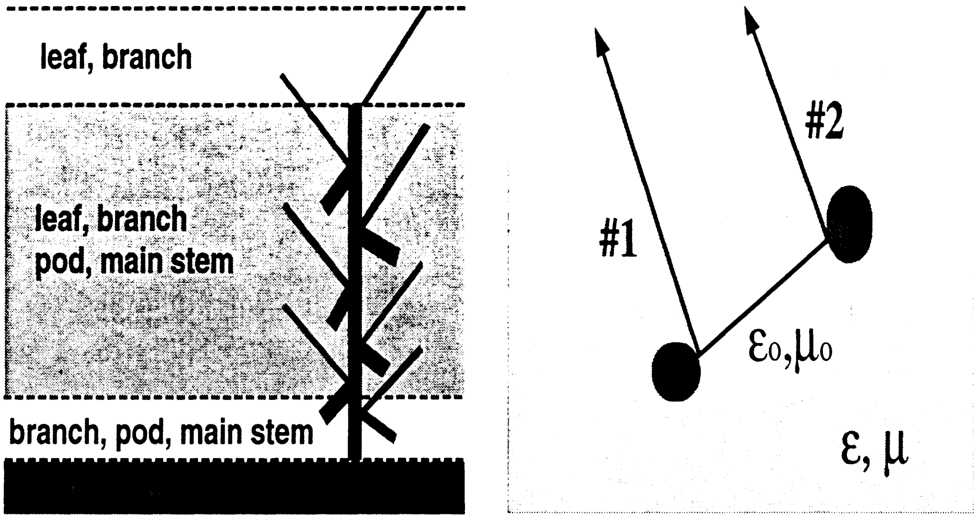

(a) (b)

Figure 4: Vegetation particles embedded in the lossy medium. (a) Stratified structure for the calculation of the equivalent propagation constant. (b) Free space is assumed in the calculation of the second-order near-field interaction.

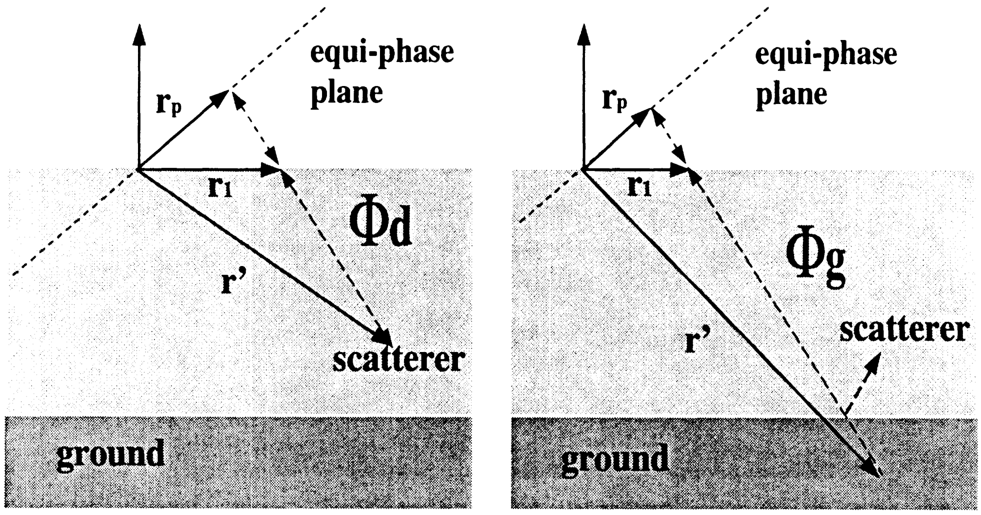

(a) (b)

Figure 5: Propagation paths in the vegetation layer. (a) direct and (b) ground bounce.

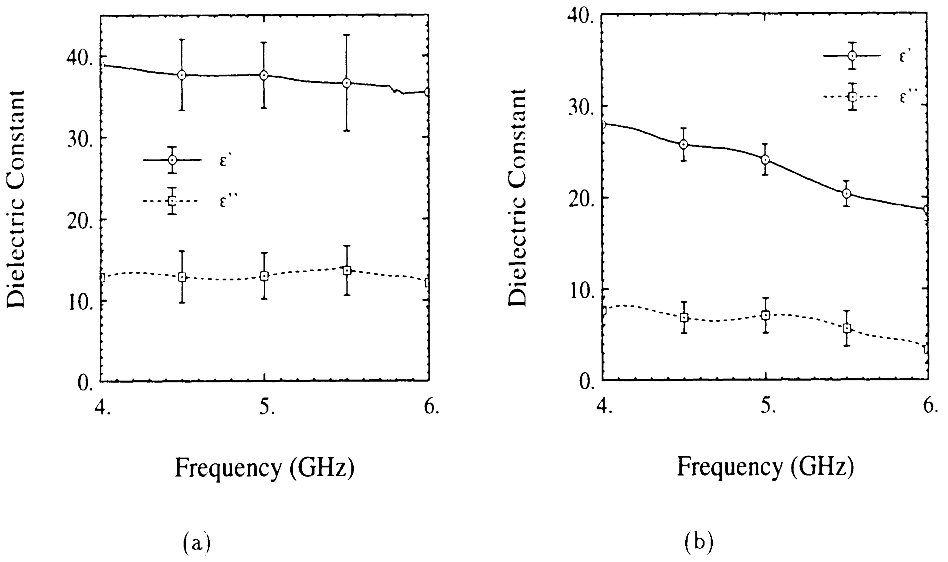

Figure 6: Measured dielectric constants for (a) branches and main stems, and (b) leaves at C-band using the procedure outlined in [24, 25].

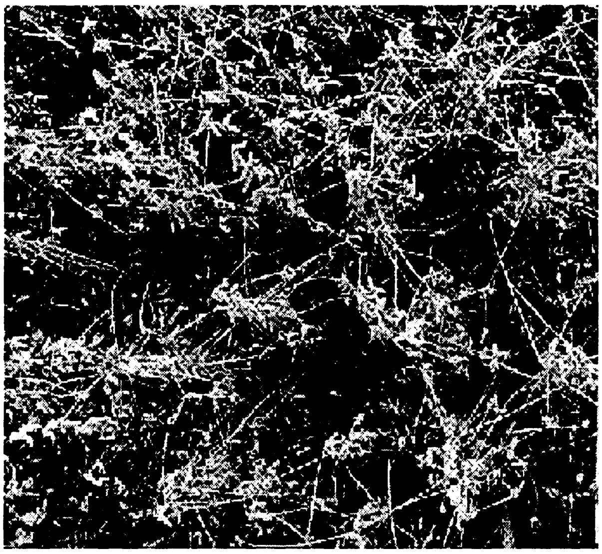

Figure 7: Picture of the soybean plant distribution for POLARSCAT data set. It was taken from the top of the field when plants were dry. Unlike the row structure which is often seen in many cultivated field, the distribution pattern is rather random.

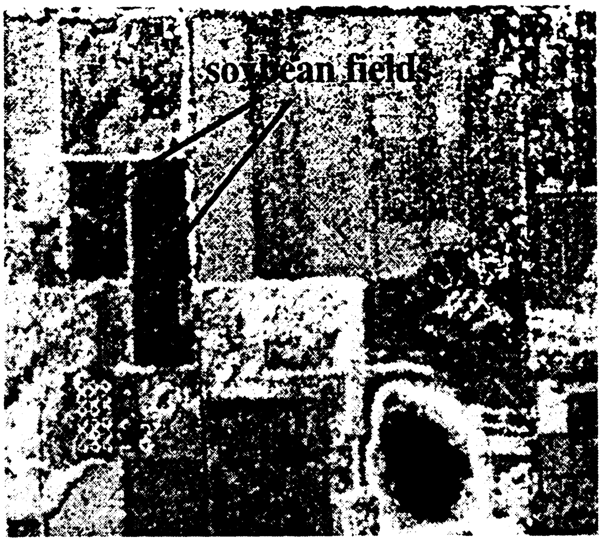

Figure 8: AIRSAR image of the Kellogg Biological Station in July of 1995. This image combined the L-band and C-band backscatter data at 45 degree of incidence angle. Two soybean field is on the left side of the image with dark color.

Figure 9: Computer-generated soybean plants for (a) POLARSCAT data set and (b) AIRSAR data set.

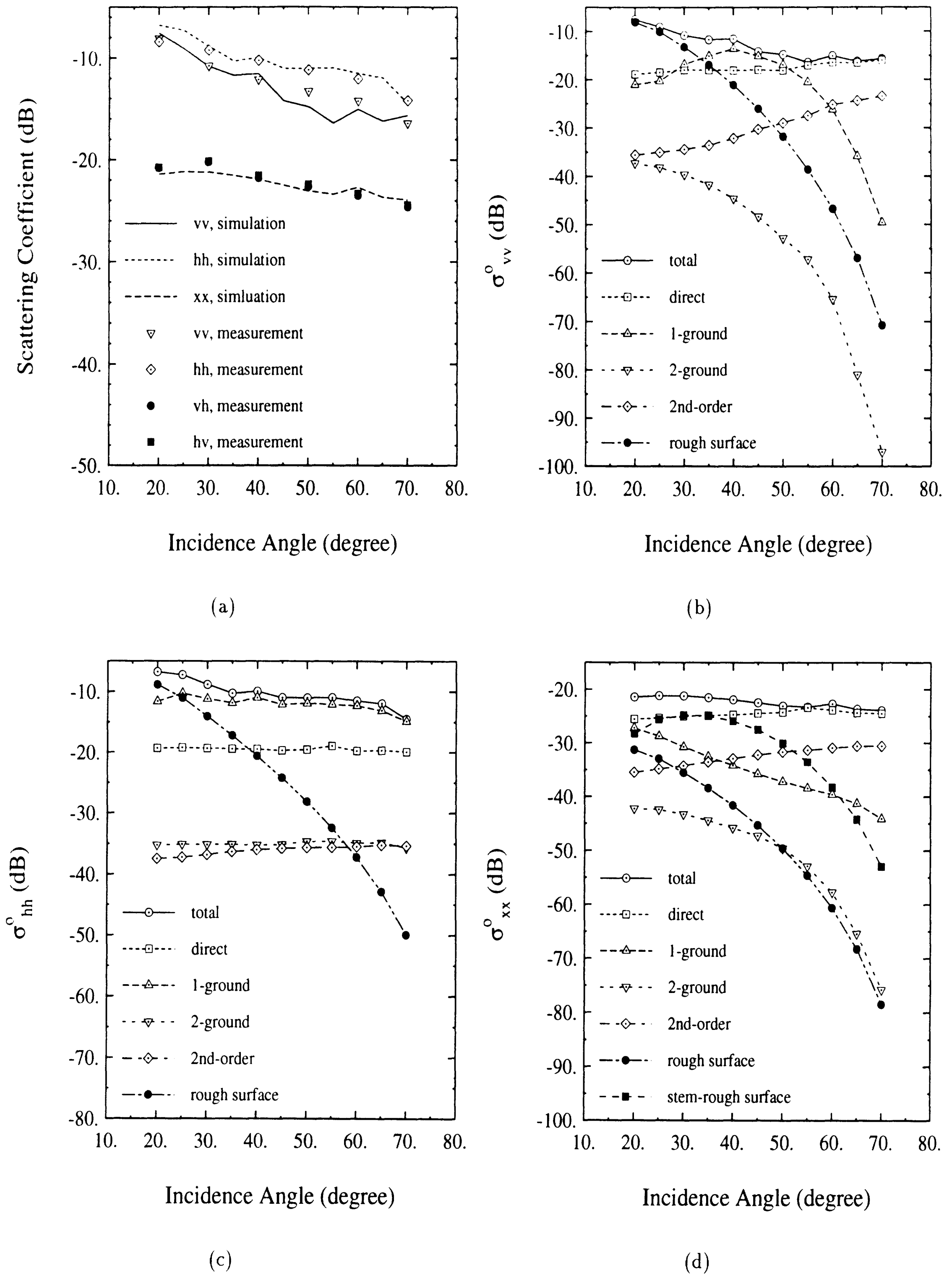

Figure 10: Scattering coefficients versus incidence angle at L-band for August 14 POLARSCAT data set: (a) model validation, and (b)(c)(d) scattering mechanism analysis for vv-, hh-, and cross-polarizations, respectively.

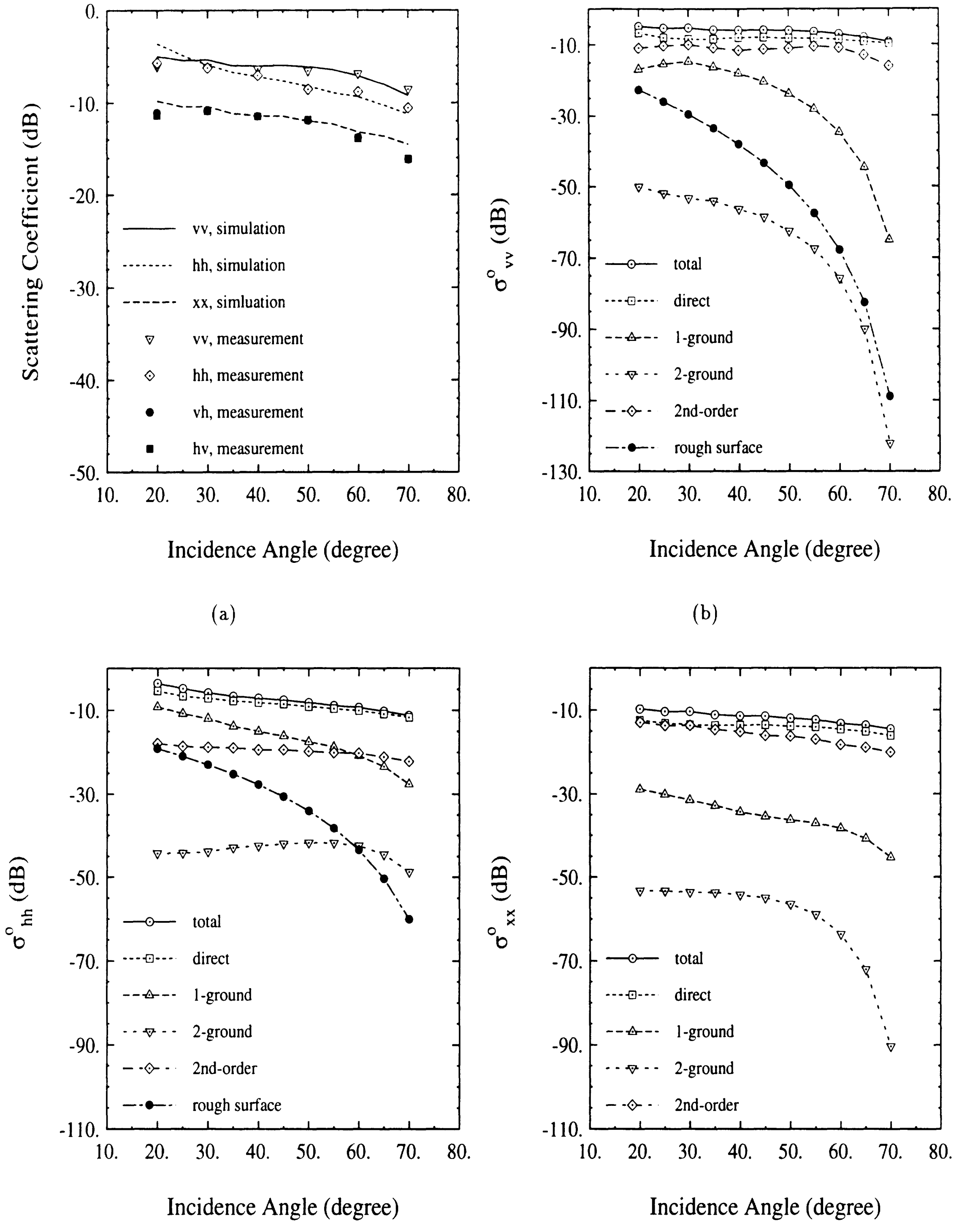

(a) (b)

(c) (d)

Figure 11: Scattering coefficients versus incidence angle at C-band for August 14 POLARSCAT data set: (a) model validation, and (b)(c)(d) scattering mechanism analysis for vv-, hh-, and cross-polarizations, respectively.

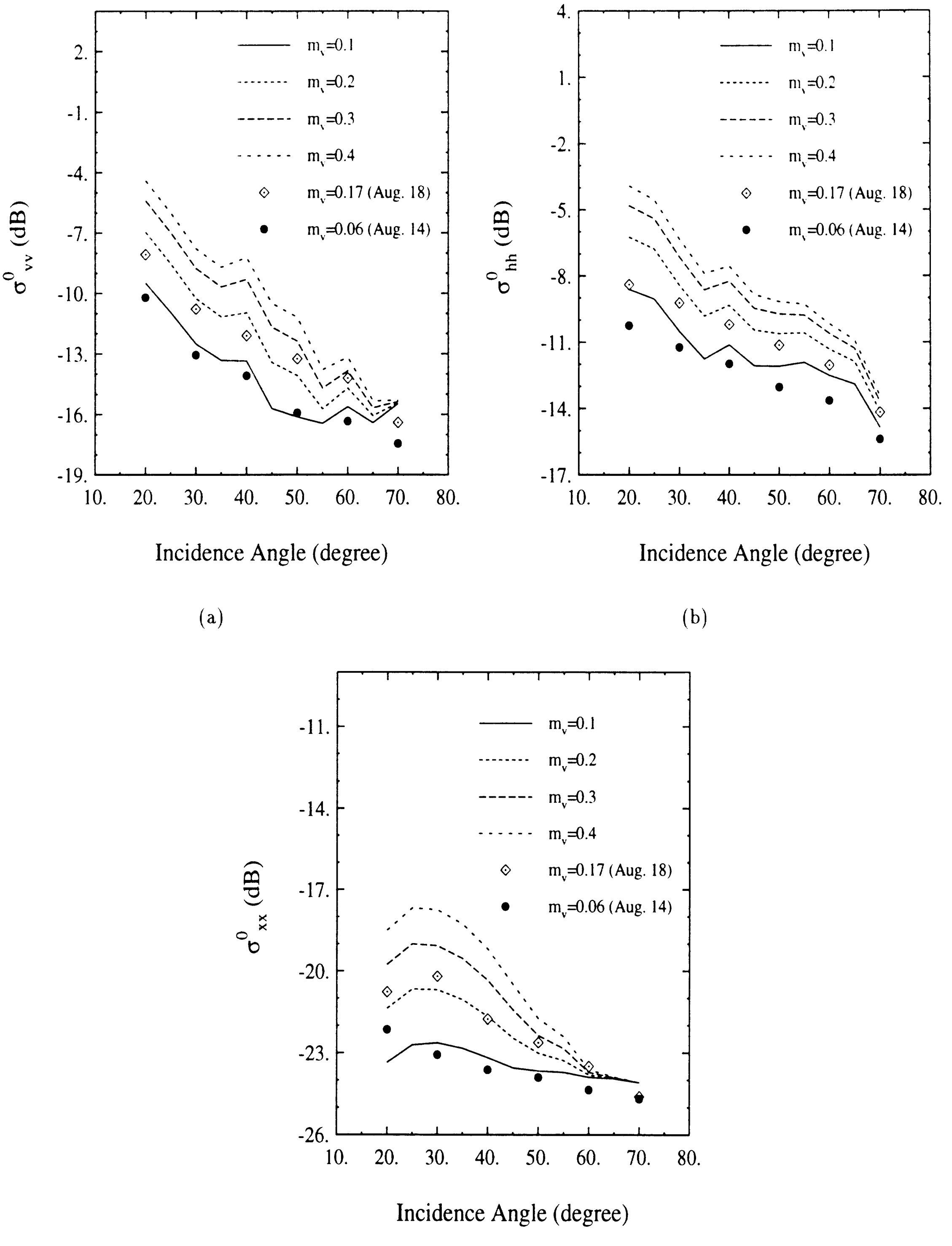

(a)

(b)

(c)

Figure 12: Analysis of sensitivity to the variation of the soil moisture for the POLARSCAT data set at L-band.(a) vv-polarization, (b) hh-polarization, and (c) cross-polarization.

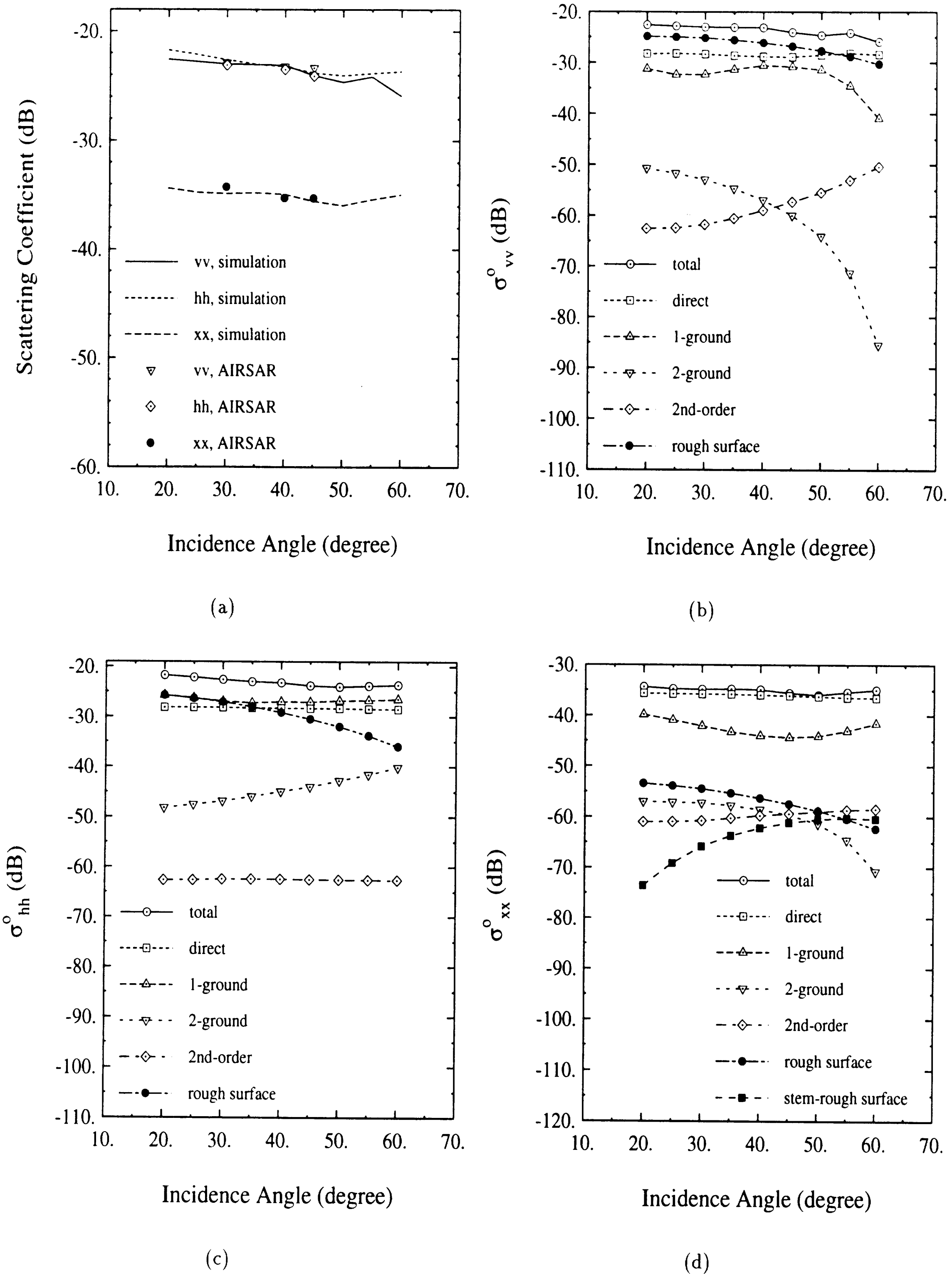

Figure 13: Scattering coefficients versus incidence angle at L-band for AIRSAR data set: (a) model validation, and (b)(c)(d) scattering mechanism analysis for vv-, hh-, and cross-polarizations, respectively.

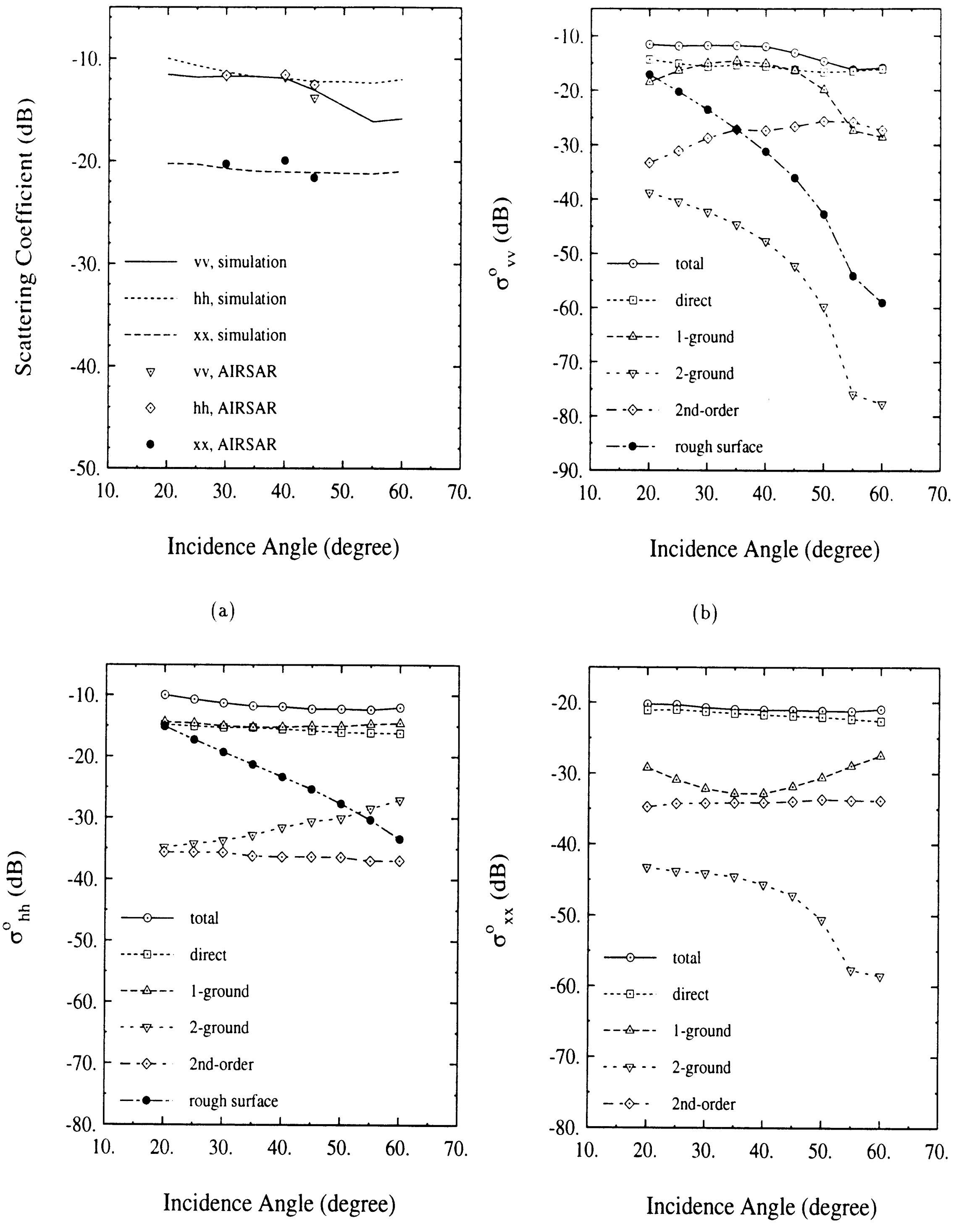

(a)

(b)

(c)

(d)

Figure 14: Scattering coefficients versus incidence angle at C-band for AIRSAR data set: (a) model validation, and (b)(c)(d) scattering mechanism analysis for vv-, hh-, and cross-polarizations, respectively.

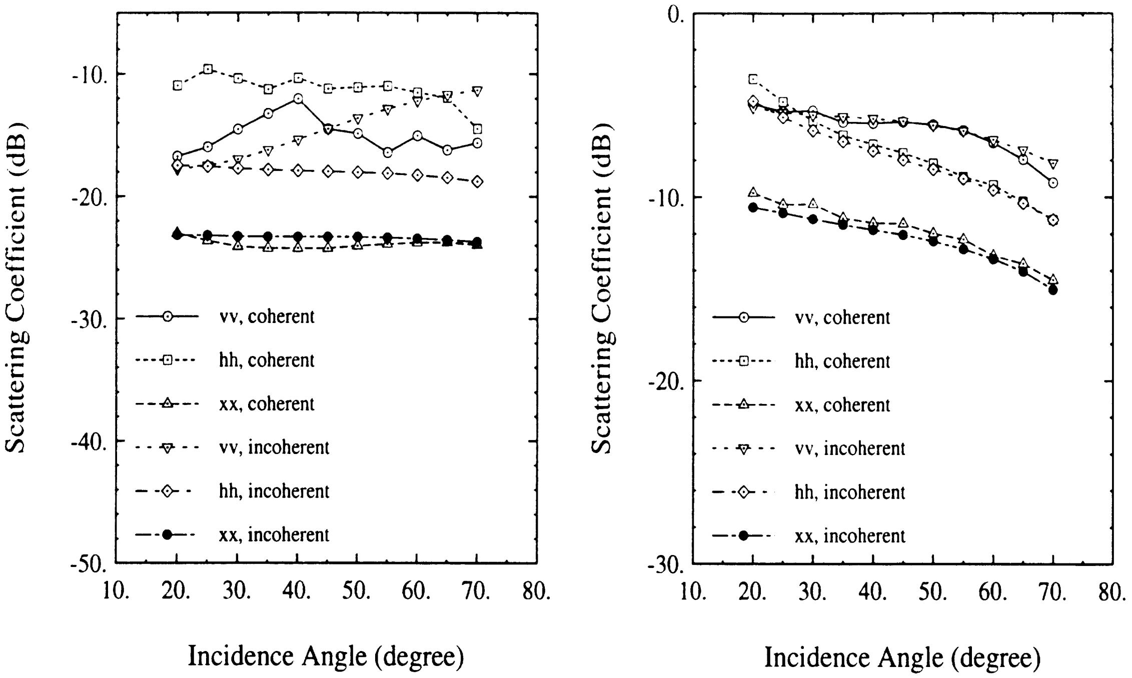

(a) (b)

Figure 15: Demonstration of the coherence effect caused by the soybean plant structure for a fully grown soybean field at (a) L-band and (b) C-band.

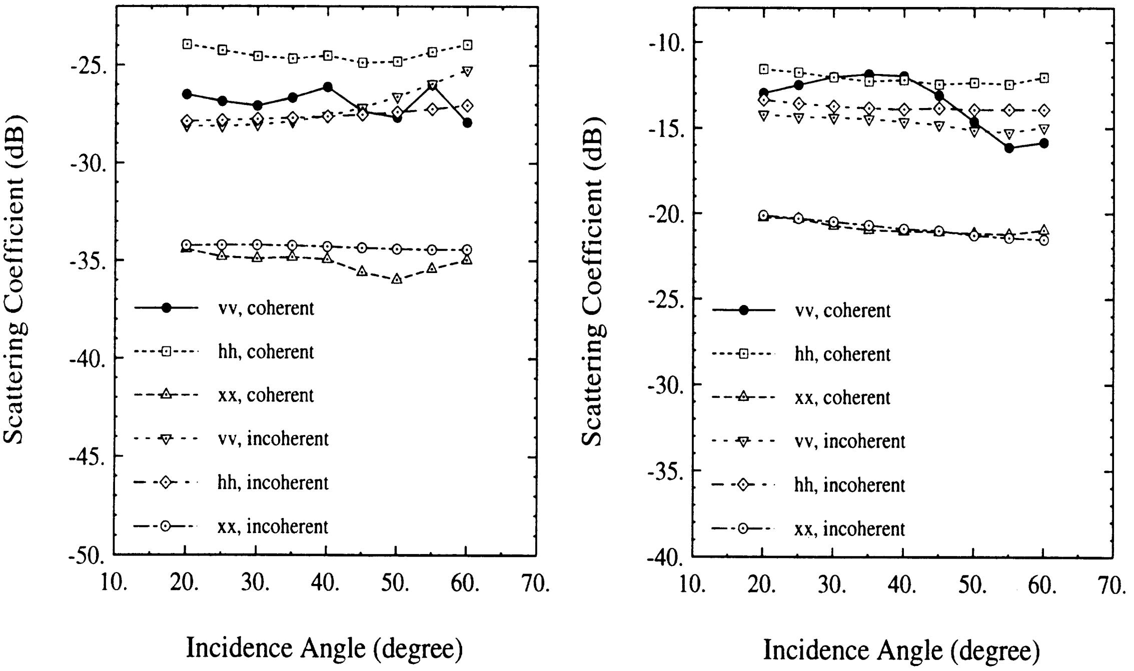

(a) (b)

Figure 16: Demonstration of the coherence effect caused by the soybean plant structure for a young soybean field at (a) L-band and (b) C-band.